

Landing Site Mapping and Lander Localization for Chang'e-5 and Chang'e-6 Lunar Sample Return Missions

Kaichang Di¹, Zhaoqin Liu¹, Wenhui Wan¹, Yexin Wang¹, Bin Liu¹, Man Peng¹, Wai Chung Liu¹, Jia Wang², Xiangjin Deng³,
Hong Zhang³, Ruiqing Sheng³, Zongyu Yue⁴, Sheng Gou⁴

¹ State Key Laboratory of Remote Sensing Science, Aerospace Information Research Institute, Chinese Academy of Sciences, Beijing, China, - (dikc, liuzq, wanwh, wangyx, liubin201656, pengman, liaowc)@aircas.ac.cn

² Beijing Aerospace Control Center, Beijing, China - 15210106156@139.com

³ Beijing Institute of Spacecraft System Engineering, China Academy of Space Technology, Beijing, China - dengxiangjin@sina.com, zhanghong122078@163.com, 50455050@qq.com

⁴ Key Laboratory of Earth and Planetary Physics, Institute of Geology and Geophysics, Chinese Academy of Sciences, Beijing, China - (yuezy, gousheng)@mail.iggcas.ac.cn

Keywords: Lunar Exploration, Landing Site, Topographic Mapping, Lander Localization, Crater Mapping.

Abstract

Chang'e-5 and Chang'e-6 are lunar sample return missions in China's lunar exploration program. In these missions, high-resolution landing site mapping and lander localization were performed to support mission operations and scientific investigations of the landing sites. The mapping and lander localization results also provided key information to provenance analysis of the samples. This paper presents a review of the landing site mapping and lander localization techniques and results in the two missions, including landing site topographic mapping using orbital images before landing, landing site topographic mapping using descent images after landing, lander localization, crater mapping and scientific applications, such as surface age determination, lunar chronology function update, and regolith thickness estimation.

1. Introduction

China's lunar exploration program, also known as Chang'e project, is divided into three phases: orbiting, landing and sample return. Since 2007, China has successfully carried out Chang'e-1 (Ouyang et al., 2010) and Chang'e-2 (Ye et al., 2013) orbiter missions, Chang'e-3 (Li et al., 2015) and Chang'e-4 (Wu et al., 2019) landed rover missions, and Chang'e-5 (CE-5) (Zhou et al., 2022) and Chang'e-6 (CE-6) (Li et al., 2024) sample return missions. In addition to remote sensing and in-situ data provided by orbiter, landers and rovers, lunar samples are of paramount importance to lunar science and have contributed significantly to our understanding of the mineralogy, geology and evolution history of the Moon (Papike et al., 1998; Meyer, 2010). Prior to the CE-5 mission, the last lunar sampling missions in Apollo and Luna programs were Apollo 17 and Luna 24, which were 48 and 44 years respectively before CE-5. Additionally, all previous Apollo and Luna missions collected samples from the near side of the Moon.

CE-5, China's first unmanned lunar sample return mission, was launched on 24 November 2020, landed in Northern Oceanus Procellarum of the Moon on 1 December 2020, and returned 1731 g samples to Earth on 17 December 2020 (Zhou et al., 2022).

CE-6 is the world's first sample return mission from far side of the Moon. Just like CE-5, CE-6 probes include an orbiter, a lander, an ascender and a returner. CE-6 was launched on 3 May 2024, landed in Apollo basin inside the South Pole-Aitken (SPA) basin on the far side of the Moon on 2 June 2024, and returned 1935.3 g samples to Earth on 25 June 2024 (Liu et al., 2024; Li et al., 2024).

We performed high-resolution landing site mapping and lander localization to support mission operations of CE-5 and CE-6

missions and various scientific investigations of the landing sites. The mapping and lander localization results also provided key information to provenance analysis of the samples. This paper presents a review of the technologies and results of landing site mapping and lander localization, and their engineering and scientific applications. Relevant work and results from some other teams are also included and cited.

2. Landing Site Topographic Mapping Before and After Landing

The landing site of CE-5 is in the Rümker region in northern Oceanus Procellarum, which experienced long and complex volcanic activity, with the eastern mare units being among the youngest mare basalts on the Moon (Qian et al., 2018). The returned samples have addressed significant issues, e.g., age and composition, lunar volcanism and thermal evolution (Che et al., 2010; Hu et al., 2021; Li et al., 2021; Tian et al., 2021). The landing site of CE-6 is in the southern basalt part of the Apollo basin. The lunar samples from this unique site are expected to address significant issues such as the ages of the SPA and the Apollo basins, mineral compositions of the lunar mantle, early impact history of the Moon, and farside volcanic history (Zeng et al., 2023; Yue et al., 2024). Landing site mapping provided the fundamental data for topographic, geomorphologic and geologic analyses of the landing sites.

2.1 Landing Site Topographic Mapping Using Orbital Images Before Landing

Due to the uncertainties in orbit and attitude measurements, imaging sensor calibration, and timing, etc., the geometric models of the orbital images, either the rigorous sensor models (RSMs) or the fitted rational function models (RFMs), are not error-free (Mazarico et al., 2012; Speyerer et al., 2016; Di et al., 2019, 2020). Lunar surface mapping directly using the original

RSMs or RFMs usually result in notable positional errors and inconsistencies among images of neighbouring orbits. Photogrammetric block adjustment technique for high-resolution lunar orbital images has been developed for large area seamless digital orthophoto map (DOM) generation, through which the geometric inconsistencies among the images of neighbouring orbits can be reduced from tens of pixels to 1 pixel level (Di et al., 2019). The systematic method consists of two major steps: RFM-based subarea planar block adjustment, and thin-plate-spline-based image registration of subarea DOMs. The first step improves the relative positional consistencies of the high-resolution images to subpixel level and ties the images to the control source (i.e., a DEM); the second step reduces the geometric inconsistencies between two neighbouring subarea DOMs and ensures the final DOM mosaic being geometrically seamless throughout the entire area (Di et al., 2019).

Based on the developed method, we produced a 1.5 m/pixel seamless DOM of the CE-5 landing area using 765 Lunar Reconnaissance Orbiter Camera (LROC) Narrow Angle Camera (NAC) images (Robinson et al., 2010), with SLDEM2015 (Barker et al., 2016) as the control source (Di et al., 2019). This high-resolution DOM covers an area of $413.8 \text{ km} \times 121.4 \text{ km}$ (see Fig.1) and has served as one of the basemaps for detailed topographic and geomorphologic analyses of the landing site before landing and for lander localization after landing.

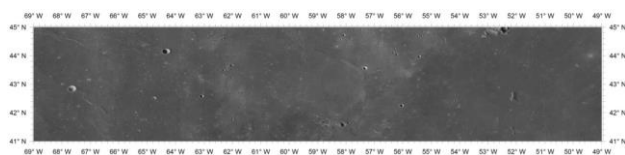


Figure 1. Seamless DOM mosaic (1.5 m/pixel) of the CE-5 planned landing area (Di et al., 2019).

For CE-6 mission, we produced a 3 m/pixel DOM ($246 \text{ km} \times 135 \text{ km}$, within the large red rectangle in the top map of Figure 2) of the pre-selected landing area using 743 LROC NAC images with SLDEM2015 as the control source. We also produced a 1 m/pixel DOM ($30 \text{ km} \times 10 \text{ km}$, the bottom map of Figure 2, corresponding to the small red rectangle of the top map) of the planned landing area using 17 LROC NAC images.

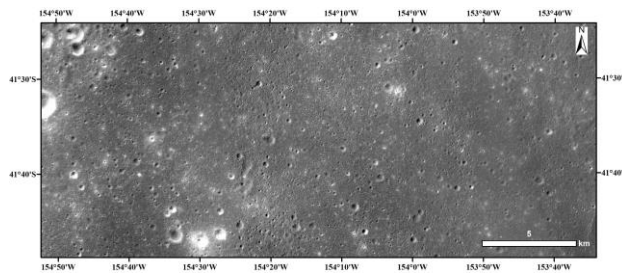
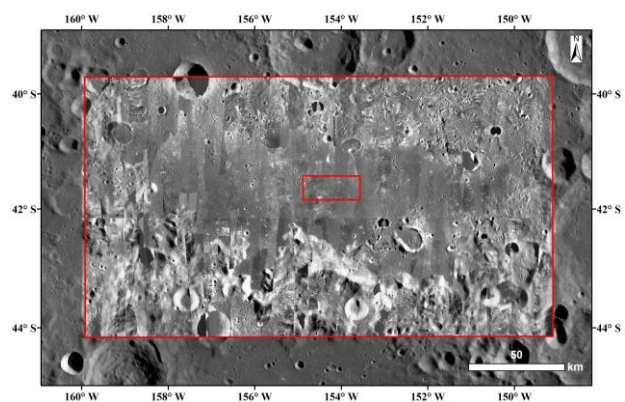


Figure 2. DOMs of the CE-6 planned landing area with 3 m and 1 m resolutions.

A 1 m/pixel digital elevation model (DEM) was generated from the 1 m/pixel DOM using shape from shading and deep learning techniques (Liu et al., 2022). Based on these maps, we performed slope analysis, crater density analysis and rock abundance analysis, to support detailed landing site selection. The DOMs were also used in lander localization after landing.

2.2 Landing Site Topographic Mapping Using Descent Images After Landing

During the descending and landing process, about 240 images with a size of 2352×1728 pixels were taken by the descent camera onboard the CE-5 lander from an altitude of 9 km until touchdown (Wang et al., 2021). Eighty-seven descent images taken from 3.9 km to 11 m altitudes were selected to generate high-resolution DOMs and DEMs (Bo et al., 2022), providing a data basis for detailed analysis of the geology and topography of the landing site, and provenance analysis of the samples (Jia et al., 2022). Figure 3 shows the DOMs 0.5 m/pixel and 0.05 m/pixel, covering $\sim 1,990 \text{ m} \times 1,900 \text{ m}$ and $\sim 260 \text{ m} \times 240 \text{ m}$, respectively. Figure 4 shows the DEM of 0.1 m grid spacing covering the same area of Figure 3a.

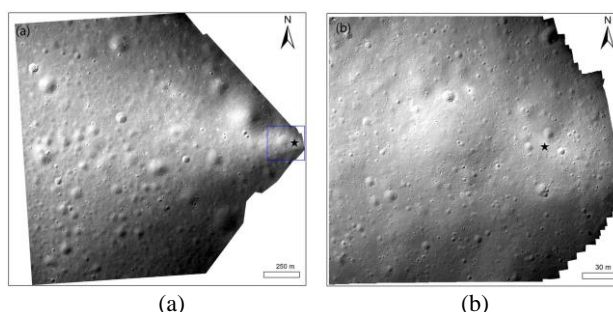


Figure 3. DOMs of 0.5 m/pixel (a) and 0.05 m/pixel (b) (corresponding to the small rectangle in (a)) in the CE-5 landing site produced from descent images (Bo et al., 2022).

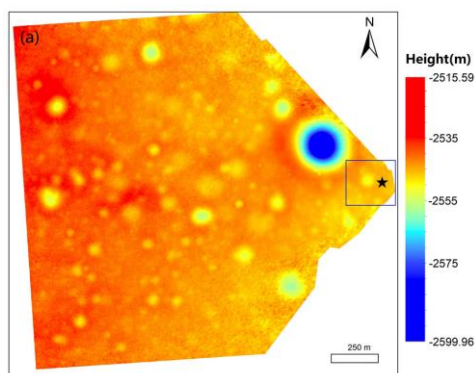


Figure 4. DEM of 0.1 m grid spacing in the CE-5 landing site produced from descent images (Bo et al., 2022).

In CE-6 mission, about 300 descent images were acquired during the descending and landing process from an altitude of about 10 km until touchdown. Sixty descent images taken from 3.9 km to 11 m altitudes were selected to generate DOMs and DEMs of the landing site with resolutions of 0.3 m and 0.03 m. These maps are being utilized for detailed crater mapping and morphologic analysis.

3. Lander Localization

Immediately after CE-5 landing, lander localization was conducted using descent images and orbital basemaps through image feature matching (i.e., visual localization). The CE-5 lander location was determined to be (51.9162°W, 43.0584°N) on the Chang'e-2 basemap and (51.9156°W, 43.0591°N) on the LROC NAC (Image ID: M1132169436LE) DOM (see Figure 5) (Wang et al., 2021). The image-based lander localization results were also compared with the radio-tracking result for cross-validation.

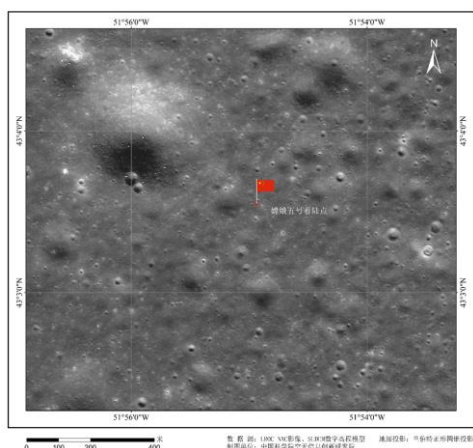


Figure 5. CE-5 lander localization result on LROC NAC basemap.

In CE-6 mission, the lander was localized through visual localization method in a fully automated manner. A new descent image simulation technique was developed based on orbital basemaps and terrain data acquired before landing to automate image matching between descent images and orbital basemaps. The location of the CE-6 lander is determined to be (153.9780°W, 41.6252°S) on the Chang'e-2 basemap, (153.9855°W, 41.6384°S) on an LROC NAC basemap (Image ID: M166854798LE) (see Figure 6), and (153.9856°W, 41.6383°S) being the average location of the lander from five LROC NAC basemaps (Liu et al., 2024).

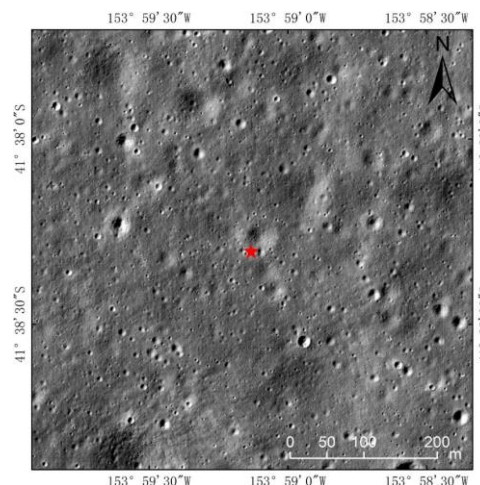


Figure 6. CE-6 lander localization result on LROC NAC basemap (M166854798LE).

The lander localization results of CE-5 and CE-6 directly supported engineering operations, e.g., planning of the ascender lifting off from the lander and subsequent maneuvers, and they are also valuable for comprehensive studies of the landing site by using remote sensing and in-site data and studies on the provenance of the samples (Wang et al., 2024; Liu et al., 2024; Yue et al., 2024).

4. Crater Mapping and Scientific Applications

Impact craters are the most abundant landforms on the lunar surface. Mapping and studying these craters provide valuable insights into the Moon's geologic history, surface evolution, and the composition of both surface and subsurface materials. As crater density is one of the critical factors to consider when selecting landing sites (Wu et al., 2020), the mapping and statistical analysis of impact craters hold significant engineering value. Several global databases of lunar impact craters larger than 1 km already exist (Robbins, 2018; Wang et al., 2021), while the extraction and analysis of smaller craters remain to be conducted based on high-resolution images.

4.1 Crater Mapping and Surface Age Determination

Before CE-5 landing, crater mapping in the landing area was conducted using the high-resolution LROC NAC basemap. The resultant crater catalogue included 174,297 craters, of which 140,796 and 32,277 craters were larger than 100 m and 200 m, respectively (Jia et al., 2020). Based on the crater catalogue, the model ages of 9 geologic units in the landing area were estimated using crater size-frequency distribution (CSFD) method (Jia et al., 2020). In relevant studies, the model ages of the geologic units estimated from CSFD are slightly different from different teams, for example, the model age of geologic unit Em4 (in which CE-5 landed) is 1.21 Ga (Qian et al., 2018), 1.49 Ga (Wu et al., 2018), and 2.07 Ga (Jia et al., 2020). This is due to differences in data source, counting area, exclusion of second craters, etc.

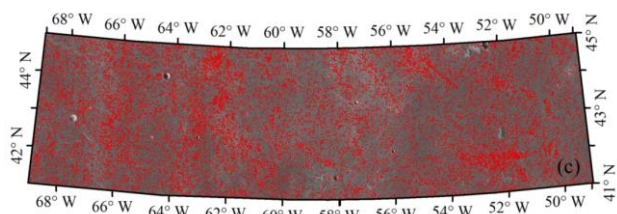


Figure 7. Mapped craters (≥ 200 m) in the CE-5 landing area overlaying on the LROC NAC DOM (Jia et al., 2020).

Using the submeter and centimeter resolution DOMs and DEMs generated from descent images, we have created a catalogue of two group of small craters in the CE-5 landing area, and most of the craters are smaller than 100 m in diameter. The first group of 7,623 craters were measured from the 0.5 m/pixel DOM with

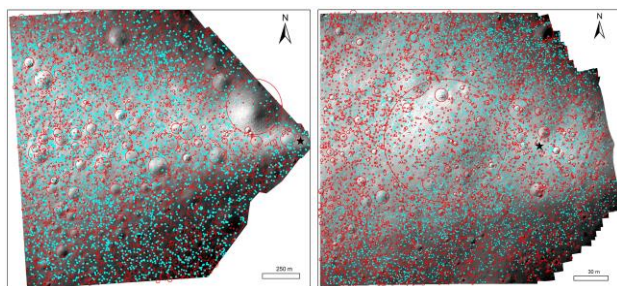


Figure 8. Distribution of all craters mapped from the 0.5 m/pixel (left) and 0.05 m/pixel DOMs (right) (Bo et al., 2022).

diameters ranging from 5 m to 371.2 m, and the second group of 11,035 craters were measured from the 0.05 m/pixel DOM with diameters ranging from 0.5 m to 112.7 m (Bo et al., 2022). The completeness diameter of the first group is ~ 6.69 m and the second one ~ 0.85 m. Figure 8 shows the mapped craters, with the ones larger than or equal to the completeness diameter being drawn with red circles and the smaller ones being drawn with blue circles.

In CE-6 landing area, a total of 770,731 craters were extracted automatically with a deep learning method (Nan et al., 2025) in the whole area of $246 \text{ km} \times 135 \text{ km}$, 511,484 craters of which were within the mare area, where CE-6 landed (Wang et al., 2024). Figure 9 shows the mapped craters (≥ 200 m) in the CE-6 landing area. The mare area was divided into three geologic units according to the TiO_2 abundance derived from spectral data, and their geologic model ages were estimated using the CSFD method (Wang et al., 2024).

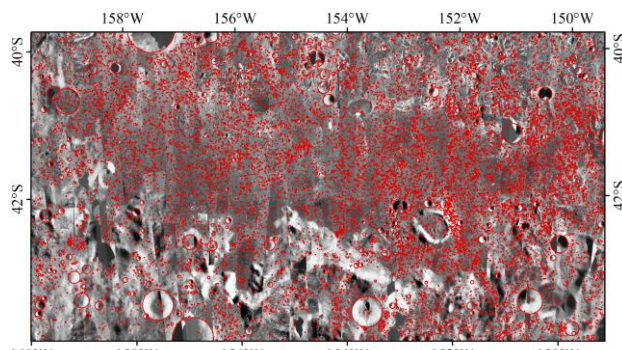


Figure 9. The mapped craters (≥ 200 m) in the CE-6 landing area overlaying on the LROC NAC DOM (Wang et al., 2024).

Several other geological and chronological analyses of the CE-5 and CE-6 landing sites have been reported by different teams with different focuses, e.g., provenance of the lunar samples, volcanism, chronology, stratigraphy, geological context etc. (Xie et al., 2020; Jia et al., 2022; Qian et al., 2024; Xu et al., 2024; Yue et al., 2024).

4.2 Lunar Chronology Function Update based on Sample Age and Crater Statistics

After CE-5 sample return and determination of the radiometric age of the basalt sample of 2.030 ± 0.004 Gyr (Li et al., 2021), the most widely used chronology model, Neukum 1983 model (Neukum, 1983), was verified and updated using the sample age and the crater size-frequency statistics (Jia et al., 2020) of the landing site, resulting a more accurate chronology model that is important for lunar surface dating and understanding of the impact history of the inner solar system (Yue et al., 2022). This new model has been included in the commonly used CSFD software CraterSats (Michael, 2021) and applied in geological and chronological studies of the Moon, e.g., geological evolution studies of the CE-5 and CE-6 landing sites (Gou et al., 2024; Qian et al., 2024; Wang et al., 2024; Xu et al., 2024; Yue et al., 2024).

4.3 Regolith Thickness Estimation from Crater Morphology

Lunar regolith is the layer of fragmented and unconsolidated material covering solid rock on the lunar surface. It holds valuable information of the geologic processes and the space environment. Regolith thickness can be estimated by the dimensions of particular craters, i.e., concentric, flat bottomed, and central mound craters (Quaide and Oberbeck, 1968; Bart et al., 2011; Di et al., 2016).

In CE-5 landing area, 958 concentric craters were identified from the high-resolution LROC NAC basemap, from which the regolith thicknesses were estimated to be 0.74 -18.00 m, with a mean of 7.15 m (Yue et al., 2019). A regolith thickness map (15 km grid) was obtained through spatial interpolation, providing important information for understanding the formation and evolution of the regolith in the landing area. Figure 10 shows the mapped concentric craters and derived regolith thickness map of the CE-5 landing area.

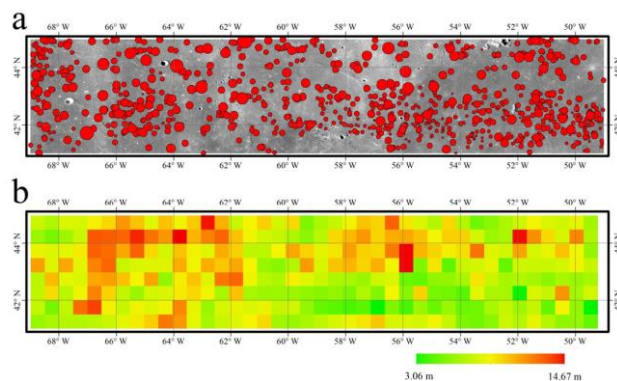


Figure 10. Distribution of concentric craters and derived median regolith thickness over the CE-5 landing area (Yue et al., 2019).

5. Conclusions

In CE-5 and CE-6 lunar sample return missions, landing site mapping (including topographic mapping and crater mapping and analyses) was conducted using orbital data and descent images before and after landing. Mapping products such as DOMs and DEMs are of meter level resolution from orbital data and submeter to centimeter resolution from descent images. Lander localization was performed by image matching between descent images and orbital basemaps, especially in CE-6 mission, automated lander localization was achieved by incorporating descent image simulation technique. The mapping and localization results have greatly supported mission operations such as landing, sampling and returning of the samples, and various scientific investigations such as surface age determination of geologic units of the landing sites, lunar chronology function update using crater statistics and radiometric age of the sample, lunar regolith estimation, etc.

Acknowledgements

The CE-5 and CE-6 missions were carried out by the Chinese Lunar Exploration Program. The authors thank the institutions/organizations for making the data used in this paper available. This work was funded in part by the National Key Research and Development Program of China (Grant No. 2022YFF0503100), and the Strategic Priority Research Program of the Chinese Academy of Sciences (grant No. XDB41000000).

References

- Barker, M. K., Mazarico, E., Neumann, G. A., et al., 2016. A new lunar digital elevation model from the Lunar Orbiter Laser Altimeter and SELENE Terrain Camera. *Icarus*, 273, 346-355.
- Bart, G.D., Nickerson, R.D., Lawder, M.T., Melosh, H.J., 2011. Global survey of lunar regolith thickness from LROC images. *Icarus*, 215, (2), 485-490.
- Bo, Z., Di, K., Liu, Z., Yue, Z., Liu, J., Shi, K., 2022. A catalogue of meter-scale impact craters in the Chang'e-5 landing area measured from centimeter-resolution descent imagery. *Icarus*, 378, 114943.
- Che, X., Nemchin, A., Liu, D., et al. 2021. Age and composition of young basalts on the Moon, measured from samples returned by Chang'e-5. *Science*, 374, 887-890.
- Di, K., Sun, S., Yue, Z., Liu, B., 2016. Lunar regolith thickness determination from 3D morphology of small fresh craters. *Icarus*, 267, 12-23.
- Di, K., Jia, M., Xin, X., Wang, J., Liu, B., Li, J., Xie, J., Liu, Z., Peng, M., Yue, Z., Liu, J., Chen, R., Zhang, C., 2019. High-resolution large-area digital orthophoto map generation using LROC NAC images, *Photogrammetric Engineering & Remote Sensing*, 85(7), 481-491.
- Di, K., Oberst, J., Karachevtseva, I., Wu, B., 2020. Topographic mapping of the moon in the 21st century: from hectometer to millimeter scales. *Int. Arch. Photogramm. Remote Sens. Spatial Inf. Sci.*, XLIII-B3-2020, 1117-1124.
- Gou, S., Yue, Z., Lin, Y., et al., 2024. Complex basalt evolution in the Chang'e-6 landing area. *Earth and Planetary Science Letters*, 648, 119091.
- Hu, S., He, H., Ji, J., et al., 2021. A dry lunar mantle reservoir for young mare basalts of Chang'e-5. *Nature*, 600, 49-53.
- Jia, B., Fa, W., Zhang, M., Di, K., Xie, M., Tai, Y., Li, Y., 2022. On the provenance of the Chang' E-5 lunar samples. *Earth and Planetary Science Letters*, 596, 117791.
- Jia, M., Yue, Z., Di, K., Liu, B., Liu, J., Michael, G., 2020. A catalogue of impact craters larger than 200 m and surface age analysis in the Chang'e-5 landing area. *Earth and Planetary Science Letters*, 541, 116272.
- Li, Q., Zhou, Q., Liu, Y., et al. 2021. Two-billion-year-old volcanism on the Moon from Chang'e-5 basalts. *Nature*, 600, 54-58.
- Li, C., Liu, J., Ren, X., et al., 2015. The Chang'e-3 mission overview. *Space Science Reviews*, 190(1-4), 85-101.
- Li, C., Hu, H., Yang, M., et al., 2024. Nature of the lunar farside samples returned by the Chang'E-6 mission. *National Science Review*, 11, nwae328.
- Liu, Y., Wang, Y., Di, K., Peng, M., Wan, W., Liu, Z., 2022. A Generative Adversarial Network for Pixel-Scale Lunar DEM Generation from High-Resolution Monocular Imagery and Low-Resolution DEM. *Remote Sensing*, 14, 5420.
- Liu, Z., Peng, M., Di, K., Wan, W., Liu, B., Wang, Y., Xie, B., Kou, Y., Wang, B., Zhao C., and Zhang Y., 2024. High-Precision Visual Localization of the Chang'e-6 Lander. *National Remote Sensing Bulletin*, 28(6), 1648-1655.
- Mazarico, E., D. D. Rowlands, G. A. Neumann, et al., 2012. Orbit determination of the Lunar Reconnaissance Orbiter. *Journal of Geodesy*, 86(3), 193-207.
- Meyer, C., 2010. Lunar Sample Compendium. The 41st Lunar Planet. Sci. Conf., abs#1016, The Woodlands, Texas.
- Michael, G.G., 2021. Planetary surface dating with craterstats3 – a new open source implementation in Python. *5th Planetary Data and PSIDA 2021*, LPI Contrib. No. 2549.
- Nan, J., Wang, Y., Di, K. Xie, B., Zhao, C., Wang, B., Sun, S., Deng, X., Zhang, H., Sheng, R., 2025. YOLOv8-LCNET: An Improved YOLOv8 Automatic Crater Detection Algorithm and Application in the Chang'e-6 Landing Area. *Sensors*, 25, 243.
- Neukum, G., 1983. *Meteorite Bombardment and Dating of Planetary Surfaces*. Habilitation thesis, Univ. Munich.
- Quaide, W.L., Oberbeck, V.R., 1968. Thickness determinations of the lunar surface layer from lunar impact craters. *J. Geophys. Res.*, 73 (16), 5247-5270.
- Ouyang, Z., Li, C., Zou, Y., et al., 2010 The primary science results from the Chang'e-1 probe. *Sci. China Earth Sci.*, 40(3), 261-280.

- Papike, J.J., Ryder, G., Shearer, C.K., 1998. Lunar samples. *Reviews in Mineralogy and Geochemistry*, 36 (1): 5–01–5–234.
- Robbins, S. J., 2018. A new global database of lunar impact craters >1–2 km: Crater locations and sizes, comparisons with published databases, and global analysis. *J. Geophys. Res. Planets*, 124(4), 871–892.
- Robinson, M., Brylow, S., Tschimmel, M., et al., 2010. Lunar Reconnaissance Orbiter Camera (LROC) instrument overview. *Space Sci. Rev.*, 150, 81–124.
- Qian, Y., Xiao, L., Zhao, S., et al., 2018. Geology and scientific significance of the Rümker region in northern Oceanus Procellarum: China's Chang'E-5 landing region. *J. Geophys. Res., Planets*, 13, 1407–1430.
- Qian, Y., Head, J., Michalski, J., et al., 2024. Long-lasting farside volcanism in the Apollo basin: Chang'e-6 landing site. *Earth and Planetary Science Letters*, 637, 118737.
- Speyerer, E.J., Wagner, R.V., Robinson, M.S., et al., 2016. Pre-flight and onorbit geometric calibration of the Lunar Reconnaissance Orbiter Camera. *Space Sci. Rev.*, 200, 357–392.
- Tian, H., Wang, H., Chen, Y., et al., 2021. Non-KREEP origin for Chang'e-5 basalts in the Procellarum KREEP Terrane. *Nature*, 600, 59–63.
- Wang, J., Zhang, Y., Di, K., Chen, M., Duan, J., Kong, J., Xie, J., Liu, Z., Wan, W., Rong, Z., Liu, B., Peng, M., Wang, Y., 2021. Localization of the Chang'e-5 Lander Using Radio-Tracking and Image-Based Methods. *Remote Sensing*, 13, 590.
- Wang, Y., Wu, B., Xue, H., Li, X., Ma, J., 2021. An improved global catalog of lunar impact craters (≥ 1 km) with 3D morphometric information and updates on global crater analysis. *J. Geophys. Res. Planets*, 126, e2020JE006728.
- Wang, Y., Nan, J., Zhao, C., Xie, B., Gou, S., Yue, Z., Di, K., Zhang, H., Deng, X., Sun, S., 2024. A Catalogue of Impact Craters and Surface Age Analysis in the Chang'e-6 Landing Area. *Remote Sensing*, 16, 2014.
- Wu, B., Huang, J., Li, Y., Wang, Y., Peng, J., 2018. Rock abundance and crater density in the candidate Chang'E-5 landing region on the Moon. *J. Geophys. Res. Planets*, 123, 3256–3272.
- Wu, B., Li, F., Hu, H., et al., 2020. Topographic and Geomorphological Mapping and Analysis of the Chang'E-4 Landing Site on the Far Side of the Moon. *Photogrammetric Engineering & Remote Sensing*, 86(4): 247–258,
- Wu, W., Li, C., Zuo, W., Zhang, H., Liu, J., Wen, W., Su, Y., Ren, X., Yan, J., Yu, D., 2019. Lunar farside to be explored by Chang'e-4. *Nature Geoscience*, 12(4), 222.
- Xie, M., Xiao, Z., Zhang, X., Xu, A., 2020. The provenance of regolith at the Chang'e-5 candidate landing region. *J. Geophys. Res. Planets* 125, e2019JE006112.
- Xu, L., Qiao, L., Xie, M., Wang, Y., Zhu, M.H., & Yan, J., 2024. Chronology, Local Stratigraphy, and Foreign Ejecta Materials at the Chang'e-6 Landing Site: Constraints on the Provenance of Samples Returned from the Moon's Farside. *Geophysical Research Letters*, 51, e2014GL11311.
- Ye, P., Huang, J., Zhang, T., Meng, L., 2013. Technology achievements of Chang'e-2 satellite and prospect of China deep space exploration. *Scientia Sinica Technologica*, 43(5), 467–477.
- Yue, Z., Di, K., Liu, Z., Michael, G., Jia, M., Xin, X., Liu, B., Peng, M., Liu, J., 2019. Lunar regolith thickness deduced from concentric craters in the CE-5 landing area. *Icarus*, 329, 46–54.
- Yue, Z., Di, K., Wan, W., Liu, Z., Gou, S., Liu, B., Peng, M., Wang, Y., Jia, M., Liu, J., Ouyang, Z., 2022. Updated lunar cratering chronology model with the radiometric age of Chang'e-5 samples. *Nature Astronomy*, 6, 541–545
- Yue, Z., Gou, S., Sun, S., Yang, W., Chen, Y., Wang, Y., Lin, H., Di, K., Lin, Y., Li, X., Wu, F., 2024. Geological context of the Chang'e-6 landing area and implications for sample analysis. *The Innovation*, 5(5), 100663.
- Zeng, X., Liu, D., Chen, Y., et al., 2023. Landing site of the Chang'e-6 lunar farside sample return mission from the Apollo basin. *Nat. Astron.*, 7, 1188–1197.
- Zhou, C., Jia, Y., Liu, J., et al., 2022. Scientific objectives and payloads of the lunar sample return mission–Chang'E 5. *Adv. Space Res.*, 69, 823–836.